ROYAL SOCIETY OF CHEMISTRY

COMMUNICATION

Check for updates

Ultralight and mechanically robust carbon monoliths with aligned microchannels

Minghao Liu,[a] Masataka Inoue,[b] Hirotaka Nakatsuji, [ID] *[a] Rui Tang,[b] Zheng-Ze Pan [ID] [b] and Hirotomo Nishihara [ID] *[ab]

While macroporous carbon materials have attracted considerable attention due to their tunable porosity, chemical and thermal stability, and electrical conductivity, they still face critical limitations in achieving a balance of ultralow density, high mechanical toughness, and efficient fluid transport through a cost-effective and environmentally friendly approach. To address these issues, an ice-templating approach is employed to fabricate ultralight yet mechanically robust carbon monoliths with aligned microchannels. By unidirectionally freezing a precursor suspension containing cellulose nanofibers and a carbon source, followed by freeze-drying and pyrolysis at 900 °C, we obtain honeycomb-like structured carbon monoliths with an ultralow density (~ 0.09 g cm^{-3}), a high compressive strength (~ 3400 kPa), and well-penetrated microchannels for efficient mass transport with minimal pressure drop. The potential of these materials is demonstrated in two key applications: high-flux water purification, achieving >99% removal of rhodamine B at an exceptional flux of 20 000 L m^{-2} h^{-1} with excellent reusability, and rapid heat exchange of flowing water, exhibiting a heat exchange efficiency four times greater than that of commercial counterparts. This study offers a versatile strategy for designing ultralight, mechanically robust, and highly permeable macroporous carbon materials with promising applications in environmental and energy-related technologies.

New concepts

This work introduces a new approach for fabricating ultralight and mechanically tough carbon monoliths with aligned microchannels. While porous carbons are extensively researched, achieving ultralow density, high mechanical toughness, and efficient fluid transport remains a major challenge. Using an ice-templating process, we combined cellulose nanofibers, phenolic resin, and carbon black to create a honeycomb-like macroporous carbon structure with aligned channels. The resulting monolith combines a low density (~ 0.09 g cm^{-3}) with a high compressive strength (~ 3400 kPa), along with efficient mass and heat transfer. This unique architecture enables high-flux (>20 000 L m^{-2} h^{-1}) water purification with over 99% RhB removal and reusability. Additionally, it demonstrated a fourfold increase in energy-efficient electrothermal heat exchange compared to commercial counterparts. The integration of structural directionality, mechanical integrity, adsorption capacity, and electrical conductivity offers a new approach for multifunctional macroporous carbons in sustainable separation and thermal systems.

1. Introduction

Macroporous materials, characterized by their large, interconnected pore structures (>50 nm), have attracted significant attention due to their unique structural properties and a broad range of applications.[1,2] These materials facilitate efficient mass and fluid transport, reduce pressure drops in fluid flow systems, and provide abundant interfacial areas for interactions between solids and fluids.[3] Applications of macroporous materials span from catalysis[4] and adsorption[5] to energy storage,[6] filtration,[7] and life science,[8] where their structural advantages play a critical role. However, traditional macroporous materials often suffer from challenges such as insufficient mechanical strength, high density, and inefficient mass transport, limiting their practical applications in fields demanding lightweight and durable solutions.

Among various macroporous materials, macroporous carbons are particularly appealing due to their exceptional properties, including chemical stability, tunable porosity, thermal stability, electrical conductivity, and thermal conductivity. These materials integrate the advantages of macroporosity, such as enhanced mass transfer and light weight, with the intrinsic benefits of carbon, including material weight, electrical conductivity, thermal conductivity, chemical inertness, thermal stability, and mechanical strength.[9–17] This combination makes them well-suited for advanced applications such as gas separation, water purification, and thermal management. For instance,

[a] Institute of Multidisciplinary Research for Advanced Materials, Tohoku University, 2-1-1 Katahira, Aoba-ku, Sendai, 980-8577, Japan.
E-mail: hirotaka.nakatsuji.d1@tohoku.ac.jp, hirotomo.nishihara.b1@tohoku.ac.jp
[b] Advanced Institute for Materials Research (WPI-AIMR), Tohoku University, 2-1-1 Katahira, Aoba-ku, Sendai, 980-8577, Japan

Wang et al.[18] reported lamellar-structured macroporous carbon rods by direct carbonization of poly tannic acid. The high porosity in the structure enhances the activity for electrocatalytic applications. Liu et al.[19] reported a phosphate-rich macroporous carbon foam for efficient uranium(VI) adsorption. It showed a high adsorption capacity due to the macroporous structure and can withstand weak acidic and basic conditions due to its carbon scaffold. Douka et al.[20] reported a macroporous carbon matrix with an interconnected pore structure. While carbon endows electrical conductivity, the three-dimensional (3D) interconnected macroporous structure maximizes the exposure of active sites and significantly enhances mass transport. Takahashi et al.[3] demonstrated carbon gel monoliths fabricated using polyester fibers as templates. They achieved straight macro-sized channels in a range of 60–160 μm, which facilitate liquid flow. By tuning the channel size, the adsorption capacity of phenol can be controlled.

Despite the progress made, existing macroporous carbon materials face several critical challenges that hinder their broader adoption. First, many macroporous carbons are still synthesized with high density, which conflicts with the requirement for lightweight materials in structural or mobile applications. Second, many macroporous carbon materials are synthesized in powder or granular forms, lacking the structural integrity needed for easier handling. Even though some research has achieved the bulk structure, brittleness remains a pervasive issue, with many materials unable to sustain mechanical stresses without structural failure. Third, the lack of open pore structures in conventional macroporous carbons results in poor fluid flow, leading to significant pressure drops and reduced operational efficiency.[21] These limitations indicate the need for innovative methods to create carbon materials that combine low density, high mechanical strength, and improved transport pathways for fluids. Developing a cost-effective and environmentally friendly manufacturing method that meets these requirements is highly desired.

To address these issues, ice templating has emerged as a versatile and promising technique for synthesizing macroporous carbon monoliths. This method utilizes the directional freezing of a suspension, where ice crystals act as templates to form aligned, interconnected pore structures.[22–25] Upon the subsequent freeze-drying process, the ice templates are sublimated, leaving behind porous materials with directional channels. It is reported that 2,2,6,6-tetramethylpiperidin-1-oxyl (TEMPO)-mediated oxidized cellulose nanofibers (CNFs)

have a remarkable ability to direct the formation of a penetrated honeycomb structure during the ice-templating process.[26] Compared with the conventional ice-templated monoliths, which typically exhibit lamellar structures, the generation of honeycomb structures using CNFs can realize the highest mechanical strength while using the minimum amount of materials.[27] These structures are characterized by a combination of low density and high mechanical strength, making them well-suited for lightweight, load-bearing materials. Additionally, the versatility in components allows for customization to meet specific needs. As a result, CNFs serve as an excellent structural guiding agent for a wide range of applications, including electromagnetic interference shielding, air filters, and batteries.[7,28–30]

Building on the promising structural role of CNFs, we present a novel macroporous carbon monolith with penetrated channels, synthesized by compositing carbon matrix precursors, such as resol-type phenolic resin (PR) and carbon black (CB), with CNFs using the ice-templating method. In this system, CNFs serve as structural directing agents, PR acts as a carbon precursor providing high mechanical strength, and CB enhances both carbonization yield and electrical conductivity. The resulting monoliths exhibit exceptional properties, combining a low density of ca. 0.09 g cm^{-1}, a high compressive strength ($\sim$3400 kPa), and well-penetrated microchannels that facilitate efficient fluid flow with minimum pressure drop. This synergistic combination overcomes key limitations of conventional porous materials, offering enhanced adsorption kinetics and improved mass transport. To highlight its practical application, the effectiveness in water purification was evaluated, achieving > 99% removal of rhodamine B at a high flux ($\sim$20 000 L m^{-2} h^{-1}) with excellent reusability. Furthermore, its performance in dynamic water heat exchange demonstrated an energy exchange efficiency of 21.4% at a water flow rate of 5 mL min^{-1}, which is four times greater than that of a commercial metal-based honeycomb monolith.

2. Results and discussion

2.1. Morphology of carbon monoliths

As illustrated in Fig. 1, a 2 wt% CNF dispersion (DKS Co. Ltd) was mixed with resol-type PR (DIC Corporation) and CB dispersion (Tokai Carbon Co., Ltd) at varying ratios. Following the
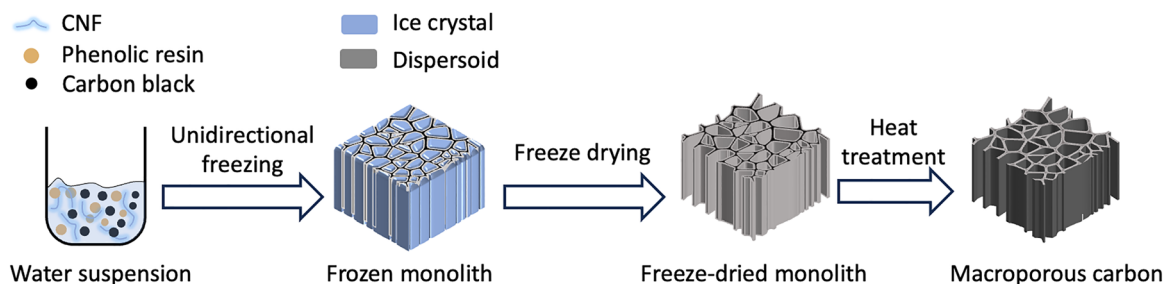

Fig. 1 Illustration of the sample preparation process.

mixing stage, the resultant precursor underwent unidirectional freezing. During this process, as the temperature reached the solidification point, the water within the dispersed mixture froze, forming ice crystals. Due to the unidirectional temperature gradient, the growing ice expelled all contaminants, including dispersed particles and polymers, and confined them within the interstitial spaces between the ice crystals.[24] Different from traditional freezing methods that directly expose the precursor to a coolant, unidirectional freezing establishes a constant unidirectional temperature gradient, enabling the aligned growth of ice crystals along this gradient. It is important to note that in most unidirectional freezing processes, ice crystals grow in lamellar shapes.[31,32] This morphology is generated from the intrinsic growth of ice, where the growth rate along the a-axis is faster than that along the c-axis (Fig. S1a), leading to lamellar-shaped ice crystals. Upon freeze-drying, sublimation of the lamellar ice left behind a lamellar-shaped framework. However, in this study, we employed CNFs as structural guiding agents to direct ice crystal growth into a parallel-aligned honeycomb structure.[33–35] As illustrated in Fig. S1b, the abundant hydroxyl groups on CNF surfaces interact strongly with water molecules via hydrogen bonding,[36] altering the dynamics of ice crystallization. Specifically, CNFs restrict the water mobility and hinder crystallization of ice in the a-axis direction. As a result, ice grows into aligned honeycomb-like arrays, rather than a lamellar structure. With the subsequent freeze-drying under low-pressure and low-temperature conditions, the ice crystals sublimated, and the macroporous monoliths with aligned honeycomb channels were obtained. The resulting ice-templated monoliths were subjected to heat treatment at 900 °C for 1 h in an N_2 atmosphere. During this process, PR first underwent cross-linking in the low temperature range, followed by pyrolysis and carbonization at high temperature, ultimately forming a 3D carbon network.

The micromorphologies of the ice-templated composites were investigated using scanning electron microscopy (SEM). Fig. 2a and b present cross-section (perpendicular to the freezing direction) SEM images of the composites obtained after the ice-templating process. The precursors were prepared with CNF : PR : CB ratios of 1 : 3 : 0 (Fig. 2a) and 1 : 3 : 3 (Fig. 2b), denoted as mPR and mPR-CB, respectively. SEM images reveal that mPR exhibits a honeycomb structure with a channel size of ca. 24 μm, indicating macroporosity. A high-magnification SEM image reveals smooth honeycomb walls. Fig. 2b indicates that mPR-CB also forms a honeycomb structure with a channel size of ca. 31 μm. Differently, the walls of mPR-CB are uniformly embedded with CB particles, with a particle size of ca. 50 nm, which is consistent with the particle-size distribution shown in Fig. S2. To verify that the honeycomb structures in mPR and mPR-CB are formed due to the structural-guiding function of CNF, a control experiment was conducted using a precursor solution containing PR and CB without CNF. As illustrated in Fig. S3, the resulting monolith exhibited a lamellar micromorphology, which is generated from lamellar grown ice in the absence of CNF. This lamellar micromorphology leads to a fragile framework that easily breaks into small pieces, as shown in the inset. In contrast, the addition of CNFs altered the ice
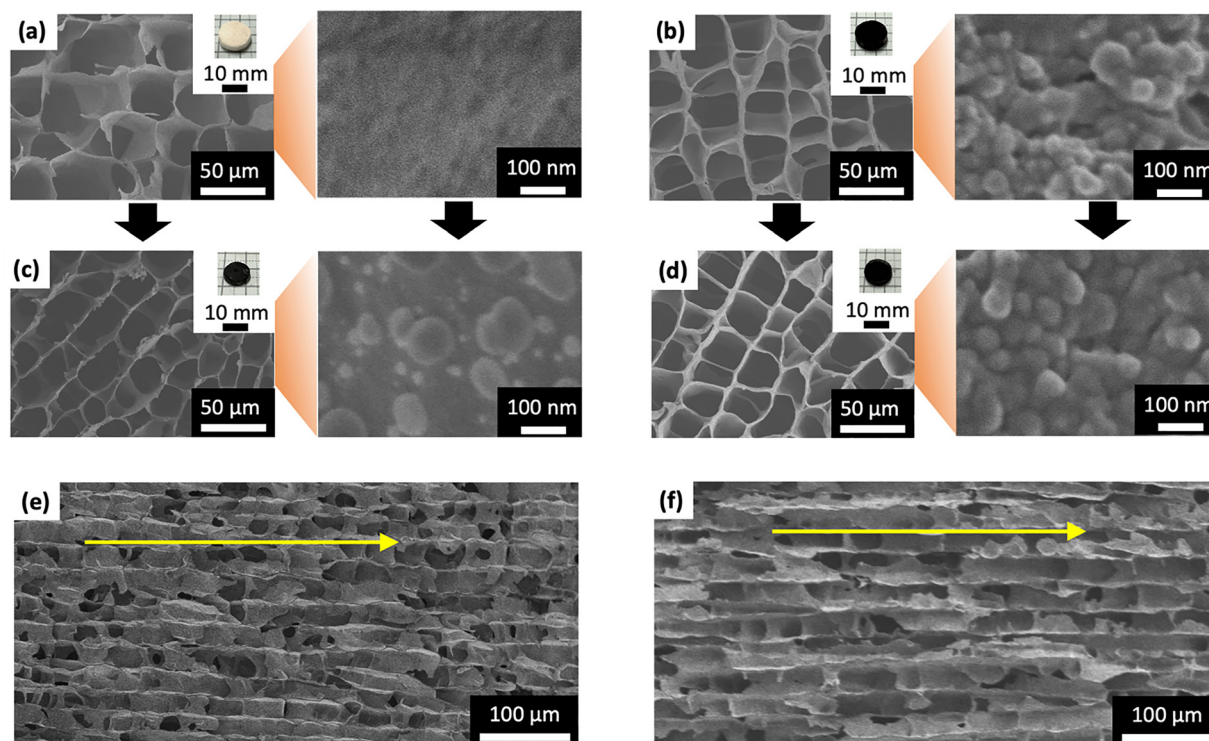

Fig. 2 Morphologies of ice-templated monoliths and their carbonized derivatives. (a)–(d) Cross-section SEM images of (a) mPR, (b) mPR-CB, (c) mPR-9, and (d) mPR-CB-9. Insets are optical images of the corresponding sample. (e) and (f) Longitudinal SEM images of (e) mPR-9 and (f) mPR-CB-9. Yellow arrows indicate the freezing direction.

growth behavior and improved mechanical stability. The failure in the control experiment underscores the necessity of CNF as a structural directing agent for forming a robust honeycomb structure. We note that freeze-drying plays a crucial role in preserving the ice-templated structure. For comparison, the unidirectionally frozen samples were directly dried in air instead of freeze-drying. As shown in Fig. S4, although the samples initially retained their shape after standing in air for 1 h, the final products exhibited severe shrinkage and structural collapse, indicating that the ice-templated framework could not be maintained. This collapse is attributed to the strong capillary forces generated during water evaporation, which impose stress on the walls. In contrast, freeze-drying avoids such forces by directly sublimating ice into vapor, preserving the aligned honeycomb channels.

Fig. 2c and d display cross-section SEM images of mPR and mPR-CB after carbonization at 900 °C, denoted as mPR-9 and mPR-CB-9, respectively. Fig. 2c shows that mPR-9 retains a honeycomb structure with a reduced channel size of $ca.$ 21 μm. The overall diameter shrinkage of the monolith was $ca.$ 23% (optical image is shown in the inset of Fig. 2c), the yield was $ca.$ 44%, and the measured density was 0.09 g cm^{-3}. A high-magnification SEM image shows particle-like structures on the surface, attributed to the carbonized product of CNF and cross-linked PR. Fig. 2d shows that mPR-CB-9 also maintains a honeycomb structure with a microchannel size of $ca.$ 25 μm. The overall diameter shrinkage of the monolith was $ca.$ 11% (an optical image is shown in the inset of Fig. 2d), the yield was $ca.$ 65%, and the measured density was 0.11 g cm^{-3}. The uniformly distributed CB particles remain unchanged in size, indicating the high thermal stability of CB. Both mPR-9 and mPR-CB-9 preserved their original micromorphologies throughout the carbonization process. This is attributed to the addition of PR and CB, as CNF alone cannot retain its shape after pyrolysis. To further validate this, an ice-templated monolith was prepared solely from a 2 wt% CNF dispersion (denoted as mCNF) as shown in Fig. S5a. After undergoing the same carbonization process, the resulting sample (denoted as mCNF-9) exhibited significant shrinkage and channel collapse (Fig. S5b), with a yield of only 17%. This collapse is due to the decomposition of CNF, highlighting the critical role of PR and CB in maintaining structural integrity. Fig. 2e and f show longitudinal SEM images of mPR-9 and mPR-CB-9, parallel to the freezing direction. Through ice-templating and heat treatment, linearly aligned channel arrays were successfully formed and maintained along the freezing direction (indicated by the yellow arrows). These aligned channels potentially offer low fluid resistance in long-range penetrated channels.

2.2. Chemical structure changes during heat treatment

The heat treatment process was comprehensively studied using thermogravimetry-differential scanning calorimetry-mass spectroscopy (TG-DSC-MS) in He and $in situ$ Fourier-transform infrared spectroscopy (FT-IR). As shown in Fig. 3a, the TG curve of mPR shows four distinct mass loss stages resulting in

a final yield of 41 wt%. These stages correspond to specific thermal reactions. (1) The initial mass loss is attributed to the cross-linking of PR, as indicated by the H_2O ($m/z = 18$) peak in the MS patterns (Fig. 3b). During this step, a condensation reaction occurs between methylene and hydroxy functional groups, releasing H_2O and forming a carbon-hydrogen 3D cross-linked structure. (2) The second stage involves the pyrolysis of CNF,[37] evidenced by the concurrent peaks of H_2O and CO_2 ($m/z = 44$). (3) The third stage involves the pyrolysis of cross-linked PR. This stage detected the release of various organic compounds, including toluene ($m/z = 91$), phenol ($m/z = 94$), cresols ($m/z = 108$), dimethylphenols ($m/z = 122$), and trimethylphenol ($m/z = 136$). The generation of phenol, cresols, dimethylphenols, and trimethylphenol is due to the scission of terminal benzene rings, while toluene production results from the dihydroxylation of these compounds.[38,39] (4) The final stage involves the carbonization process, accompanied by the release of methane ($m/z = 16$). During this stage, the methylene scission decomposes, leading to the formation of char with direct aromatic–aromatic links.[40] The $in situ$ FT-IR spectra (Fig. 3c) provide detailed chemical structure changes during the pyrolysis process of mPR. The original monolith showed a characteristic peak at 1065 cm^{-1} (highlighted in green) derived from C–H stretching of CNF.[41] Peaks at 1250–1300 cm^{-1} (phenolic –OH deformation, C–O stretching of the phenol group, or biphenyl ether structure), and 1125 cm^{-1} (polycyclic aromatic ring deformation and alkyl-phenolic C–O stretching), highlighted in red, are derived from PR.[39,40] Peaks at 3500 cm^{-1} and 2963 cm^{-1}, highlighted in blue, correspond to O–H stretching vibrations of hydroxy groups and C–H stretching, derived from both CNF and PR.[41–44] As the temperature increases to 300 °C, CNFs decompose, resulting in the disappearance of the 1065 cm^{-1} peak. Upon further heating to 600 °C, all characteristic peaks disappear, indicating complete carbonization. The results demonstrate that PR plays the key role in the pyrolysis process. The cross-linking of PR via condensation reactions leads to a rigid three-dimensional polymeric network. This cross-linked network solidifies the honeycomb framework and provides structural integrity.

Fig. 3d and e illustrate the TG curve and MS patterns for the heat-treatment process of mPR-CB. Similar to mPR, it also experiences four stages: cross-linking of PR, pyrolysis of CNF, pyrolysis of PR, and carbonization. However, mPR-CB shows a higher yield of 63 wt%, due to the presence of CB. Fig. 3f depicts the $in situ$ FT-IR spectra of the pyrolysis process of mPR-CB. In contrast to the pyrolysis behavior of mPR, a characteristic C–O–C peak at 991 cm^{-1} (highlighted in yellow) emerges between 100 and 400 °C. This suggests the formation of chemical bonding between CB and PR.[45] The CB used in this study was surface-modified to achieve high dispersibility, introducing –OH and –COOH functional groups (the FT-IR spectrum is shown in Fig. S6). Upon heating, CB does not undergo polymerization by itself; instead, the functional groups on the CB surface participate in the reaction with PR, leading to covalent bonding or grafting of PR on the CB surface.
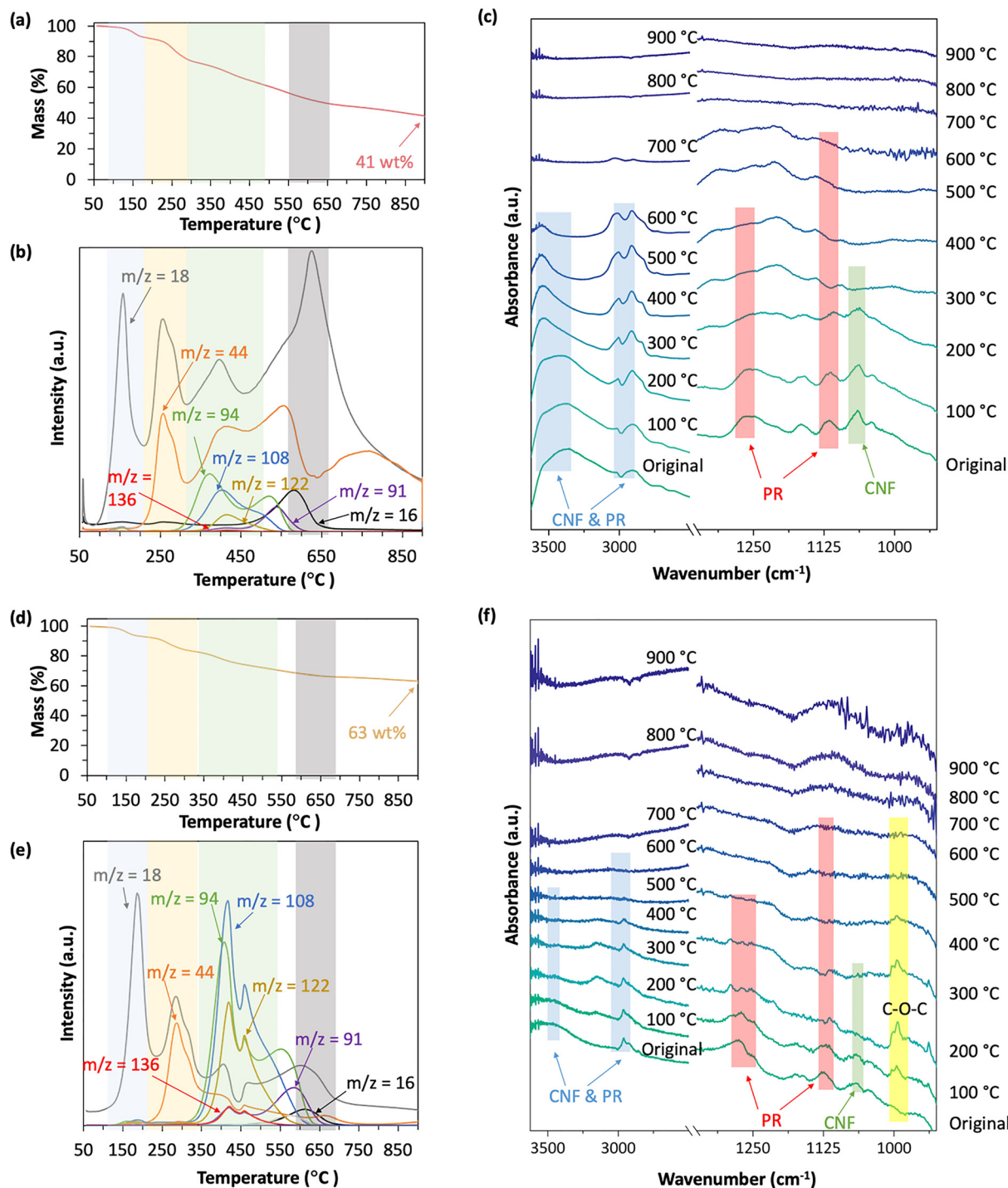
Fig. 3 The chemical structure change of (a)–(c) mPR and (d)–(f) mPR-CB during heat treatment. (a) and (d) TG curves in He, (b) and (e) MS patterns, and (c) and (f) *in situ* FT-IR spectra.

The intrinsic –OH groups in PR can interact with the –OH and –COOH groups on CB through dehydration condensation, forming C–O–C bonds. This competitive reaction disrupts the direct cross-linking between PR molecules, altering the network structure of the composite. However, a large portion of PR still undergoes condensation to form the rigid 3D network. This ensures that the honeycomb structure remains strong enough to survive the heat treatment, even with CB present. Therefore, PR still serves as the most important for maintaining the mechanical integrity.

2.3. Mechanical properties of carbon monoliths

The mechanical toughness of the as-prepared monoliths was evaluated by a universal testing machine. All specimens were
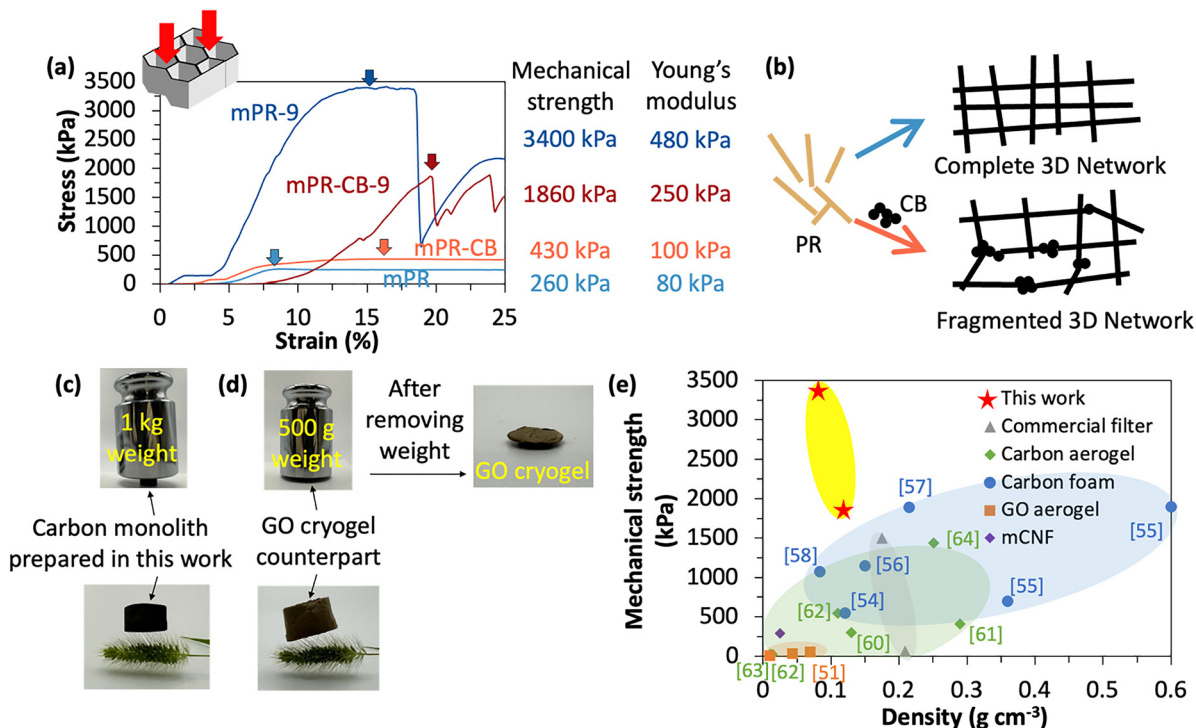
Fig. 4 Mechanical properties of carbon monoliths. (a) Axial compression stress–strain curves of mPR, mPR-CB, mPR-9, and mPR-CB-9. Arrows indicate the fracture points for each sample. The inset illustration indicates the compression direction. (b) Illustration of the cross-linking of PR in the absence (upper) and presence (bottom) of CB. (c) Optical images demonstrating the exceptional mechanical properties of mPR-CB-9: it is strong enough to support a 1 kg weight (upper) and light enough to place on a foxtail (lower). (d) Optical images show that a GO aerogel demonstrates its mechanical limitations: it cannot withstand a weight of 500 g, collapsing under the load (upper) although it is lightweight (lower). (e) Comparison of axial compression strength of the carbon monoliths prepared in this study with other porous monoliths. Reference numbers are indicated in the form of [X] in the figure.[51,54–58,60–64]

compressed to 80% deformation at a 100% strain min^{-1} compression rate to obtain stress–strain curves. The stress–strain curves obtained by compressing from the axial direction are depicted in Fig. 4a. Initially, all samples underwent a linear increase in stress with increasing strain. Upon reaching the strength limit, the stress dropped suddenly, indicating the samples either cracked or condensed. The peak stress, indicated by an arrow, represents the compression strength. The compression strengths of mPR and mPR-CB were 260 kPa and 430 kPa, respectively, and Young's moduli were 80 kPa and 100 kPa, respectively. The higher compression strength and Young's modulus of mPR-CB is attributed to the higher solid content of the precursor, which increases the wall thickness of the macroporous walls.[22] The mechanical strength of the monolith was substantially enhanced through carbonization. mPR-9 and mPR-CB-9 show compression strengths of 3400 kPa and 1860 kPa, respectively, and Young's moduli of 480 kPa and 250 kPa, respectively (Fig. S7). The substantial enhancement in mechanical strength suggests that the cross-linked PR polymer undergoes transformation into graphene-like carbon layers, which interconnect to form a robust and mechanically stable 3D framework.[46] Interestingly, mPR-CB-9 showed lower compression strength compared to mPR-9, contrary to the trend observed in mPR and mPR-CB. To better understand this effect, high-resolution SEM was conducted to obtain nanoscale

information (Fig. S8). For mPR-9, similar to the result shown in Fig. 2, the surface appears wrinkled with occasional larger particles. This suggests that PR undergoes a relatively uniform cross-linking and carbonization, resulting in a continuous carbon layer. In contrast, the addition of CB disrupts the homogeneity of this transformation. The surface of mPR-CB-9 is uniformly decorated with CB across the carbonized matrix. Although these CB particles introduce additional nanoscale roughness and potential microporosity, the presence of CB also introduces discontinuities within the carbon framework (Fig. 4b).[47,48] Under external mechanical load, stress concentration occurs at these interfaces, thus resulting in particle sliding. Consequently, the compressive strength is reduced compared to the more homogeneous carbon network of mPR-9.

Stress–strain curves for radial compression are depicted in Fig. S9. Different from axial compression, radial compression curves do not exhibit a distinct stress drop. Instead, they show a continuous stress increase until the material is densified. The compression strengths of mPR, mPR-CB, mPR-9, and mPR-CB-9 are 110 kPa, 180 kPa, 320 kPa, and 380 kPa, respectively. Heat treatment led to an increase in strength, and the trend was consistent with the axial compression results. Additionally, densification occurred at lower stress levels compared to those observed in axial compression. This is because honeycomb structures exhibit greater stiffness and strength under axial

compression due to the alignment of cell walls with the applied load.[49,50]

Although the incorporation of CB reduced the compression strength and increased the density of the carbon monolith, it remained sufficiently strong to withstand external forces while maintaining a lightweight structure. As displayed in Fig. 4c, a 1 kg weight was placed on mPR-CB-9, and it can be visibly seen that the monolith can support the load without deformation. Meanwhile, it also shows that the monolith can be placed on a delicate plant (a foxtail) without causing any visible deformation of its soft hairs, highlighting its lightweight nature. In contrast, we prepared a graphene oxide (GO) aerogel counterpart[51] using the same ice templating method as for the carbon monolith. The GO aerogel exhibited an ultra-low density of *ca.* 0.01 g cm^{-3} but exhibited a significantly lower mechanical strength of 6 kPa. As displayed in Fig. 4d, the GO aerogel could also be placed on a foxtail, demonstrating the lightweight property. However, when a 500 g weight was placed on the GO aerogel, unlike mPR-CB-9, the GO aerogel was completely compressed under the load, indicating its significantly lower mechanical strength. The weak mechanical performance of GO aerogels is attributed to their intrinsic chemical and structural features. GO sheets are primarily connected through non-covalent interactions, such as π–π stacking, hydrogen bonding, and electrostatic interactions,[52] which provide insufficient structural integrity. These weak iterations lead to a fragile and poorly connected 3D porous framework. Furthermore, the abundant negatively charged functional groups on GO sheets induce strong electrostatic repulsion. This further hinders sheet-to-sheet contact during the freezing process, finally decreasing the structural integrity of the aerogel.[53] By contrast, both mPR-9 and mPR-CB-9 benefit from the cross-linking of PR, which contributes to its high strength and resistance to deformation.

To confirm the surpassing mechanical properties of the monoliths prepared in this work, we compared the compressive strength (axial direction) and density with commercial products (a ceramic filter and a water filter), GO aerogel counterpart, carbon foams,[54–58] and carbon aerogels.[59–64] As illustrated in Fig. 4e, the carbon aerogels (green region) exhibit exceptionally low density, making them attractive for applications requiring lightweight materials. However, their mechanical strength is significantly limited, restricting their usability in high-pressure environments. On the other hand, carbon foams (blue region) offer enhanced mechanical strength, yet their higher density hinders their applications where lightweight structures are critical. The existing commercial filters (gray region) demonstrate moderate mechanical properties, but they fail to optimize the balance between low density and high strength, limiting their high performance. Meanwhile, the GO aerogel prepared in this work displayed extremely low mechanical strength, which limits its potential for widespread applications. In contrast, mPR-9 and mPR-CB-9 (yellow region) overcome these limitations by achieving a combination of low density and superior mechanical strength. This breakthrough significantly expands the application potential, making them ideal for a wide range of

next-generation technologies, including but not limited to lightweight structural materials, filtration systems, and heat management devices.

2.4. Water purification performance

Based on the advantage of the efficient fluid pathways offered by the penetrated channel arrays and the high mechanical properties endowed by the developed 3D graphene network, they are versatile in various applications. An example is water purification. In recent years, many advanced porous materials have been developed to enhance water purification performance.[65–68] Despite the improved purification performances, there is a problem with these research results: the removal of pollutants is either requested over a long time or performed at a low flux, which increases time consumption and decreases efficiency. Given these challenges, there is a critical need for innovative solutions that can provide fast and efficient removal of water pollutants.

Fig. 5a displays the N_2 adsorption/desorption isotherms of mPR, mPR-CB, mPR-9, and mPR-CB-9. The specific surface areas (SSAs) of mPR and mPR-CB that were calculated using the Brunauer–Emmett–Teller (BET) method (S_{BET}) were 3 m^2 g^{-1} and 4 m^2 g^{-1}, respectively, indicating low SSAs before heat treatment. Although CB exhibits an S_{BET} value of 124 m^2 g^{-1} with mesoporosity (Fig. S10), the S_{BET} value of mPR-CB remains low. This reduction is attributed to the ice-templating process, where non-porous CNFs and PR adhere to the CB surface, reducing the accessible surface area. The S_{BET} values of mPR-9 and mPR-CB-9 were 2 m^2 g^{-1} and 108 m^2 g^{-1}, respectively. While mPR-9 still exhibited an extremely low SSA, suggesting a non-porous structure of carbonized PR, mPR-CB-9 showed increased porosity. The significantly increased SSA of mPR-CB-9 indicates a higher porosity, which can be attributed to the heat treatment. We note that although the SSA achieved in this work is moderate compared to nanoporous carbons, the powerful structural guiding ability of CNF allows us to incorporate additional functional components to enhance the SSA and adsorption capacity if required.

The pollutant removal tests were conducted using Rhodamine B (RhB) as a model solution. RhB is widely used for leather, dye lasers, and fluorescent tracers (the molecule structure is depicted in Fig. S11a).[69,70] It is particularly concerning due to its toxicity and non-biodegradability. Exposure to such pollutants potentially causes liver and thyroid damage, as well as carcinogenic effects. Therefore, the removal of RhB from water sources is critically important for protecting human health. The concentration of RhB used in this work was analysed by ultraviolet-visible (UV-Vis) spectroscopy at a wavelength of 554 nm (Fig. S11b), and the calibration curve is shown in Fig. S11c. Initially, we evaluated the RhB adsorption capacity of both mPR-9 and mPR-CB-9. Samples were crushed into powder and introduced to RhB solutions at six different concentrations. The samples were stirred for 72 h to reach adsorption equilibrium. The residual RhB concentrations were determined using UV-vis spectroscopy (see Section 4.4 for experimental details), and the adsorption isotherms (Fig. 5b)
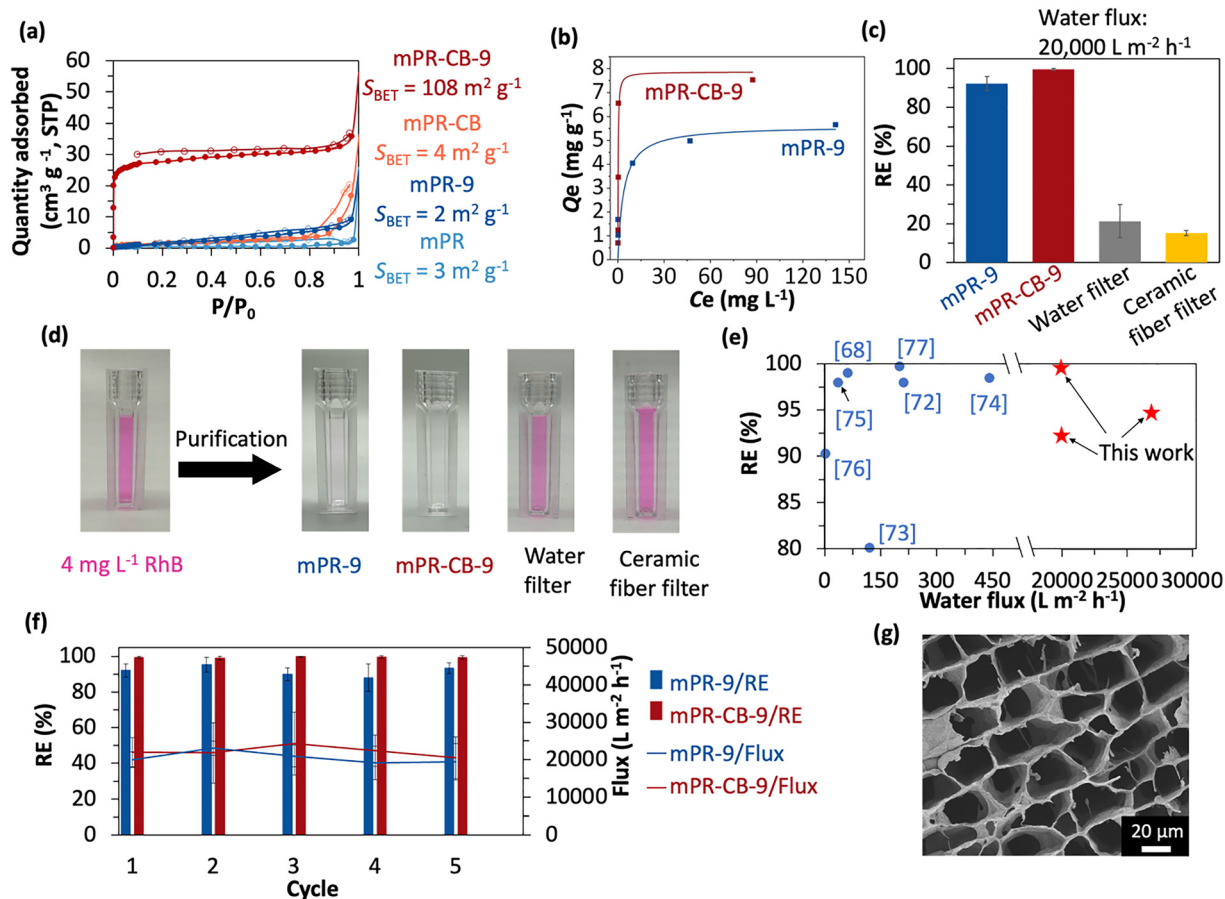
Fig. 5 Porosity evaluation and water purification performance of carbon monoliths. (a) N$_2$ adsorption–desorption isotherms of mPR, mPR-CB, mPR-9, and mPR-CB-9. (b) Adsorption isotherms and associated Langmuir fits (solid lines) for mPR-9 and mPR-CB-9. (c) RhB RE results of mPR-9, mPR-CB-9, the commercial water filter, and the commercial ceramic fiber filter. (d) Optical images of the RhB solutions before and after purification by mPR-9, mPR-CB-9, the commercial water filter, and the commercial ceramic fiber filter. (e) Performance comparison with other RhB purification studies. (f) RhB RE and flux of mPR-9 and mPR-CB-9 after consecutive regeneration cycles. (g) SEM image observed along the axial direction of mPR-CB-9 after five cycles of regeneration.

were fitted to a Langmuir model to calculate the maximum capacity (Q_m [mg g^{-1}]). The Q_m values of mPR-9 and mPR-CB-9 were 5.6 mg g^{-1} and 7.9 mg g^{-1}, respectively.

The RhB purification tests were conducted using a setup illustrated in Fig. S12. A sample with a diameter of $ca.$ 15 mm and a thickness of $ca.$ 8 mm was fixed on a sample holder. Then, a syringe containing RhB solution ($ca.$ 4 mg L^{-1}) was used to inject the liquid into the sample holder at a water flux of over 20 000 L m^{-2} h^{-1}. Fig. 5c illustrates the RhB removal efficiency (RE [%]). Notably, compared to most existing studies, where water fluxes are typically below 1000 L m^{-2} h^{-1}, the water flux achieved in this work is over 20 times higher. The RhB RE of mPR-9 and mPR-CB-9 reached 92.1% and 99.4% at a water flux of $ca.$ 20 000 L m^{-2} h^{-1}, whereas two commercial filters (a water filter and a ceramic fiber filter) only achieved RhB RE below 20%. Fig. 5d presents the optical images of RhB solutions before and after purification. After treatment with mPR-9 and mPR-CB-9, the RhB solution became transparent, however, the commercial filters failed to remove the dye, leaving the RhB solution visibly colored. For mPR-9, experiments were

conducted not only at 20 000 L m^{-2} h^{-1} but also at 27 000 L m^{-2} h^{-1}, and the RE was 94.7%, indicating that the increased water flux did not compromise the removal efficiency. The results of purification tests are consistent with Q_m. It is noteworthy that despite mPR-9 showing much lower SSA, it still effectively removed RhB. This suggests that adsorption capability depends on an extensive macropore surface area (S_{macro}), which corresponds to the exposed surface of honeycomb walls. To quantify this effect, S_{macro} is calculated using the following eqn (1).

$$S_{macro} = \frac{S}{\pi\left(\frac{d+t}{2}\right)^2} \times \pi dL \tag{1}$$

where S_{macro} is the total macropore surface area, S is the cross-section area of the monolith, d is the microchannel diameter, t is the honeycomb wall thickness, and L is the length of the carbon monolith.

The S_{macro} value of mPR-9 was calculated to be $ca.$ 0.23 m^2, significantly exceeding the area occupied by RhB at adsorption saturation following the Langmuir equation (0.053 m^2),

assuming the molecular size of RhB is 1.344×1.207 nm^2. This confirms that the available S_{macro} of mPR-9 is sufficient for effective RhB removal. The adsorption of RhB is driven by π–π interactions between the graphitic carbon backbones and the aromatic rings of RhB molecules,[71] enhancing adsorption efficiency even without extensive microporosity. mPR-CB-9 exhibited higher FE than mPR-9 due to increased microporosity and SSA introduced by CB incorporation, which provides more adsorption sites and enhances overall capacity. A performance comparison with other RhB adsorption studies is shown in Fig. 5e.[68,72–77] Notably, our study achieves a significantly higher water flux than previously reported studies while maintaining a high RE for RhB, overcoming the conventional trade-off between permeability and contamination removal.

Beyond efficiency, reusability is crucial for economic feasibility. The reusability of carbon monolith was demonstrated at a water flux of *ca.* 20 000 L m^{-2} h^{-1}. Both mPR-9 and mPR-CB-9 were easily regenerated using 10 mL of ethanol followed by 10 mL of water. Over five RhB purification/regeneration cycles, no significant performance degradation was observed (Fig. 5f). The SEM image observed after five cycles (Fig. 5g) shows that the honeycomb structure remained intact, indicating excellent mechanical and chemical resistance during both the purification and regeneration processes. We also examined the mechanical stability after five cycles. The decline in compressive strength after the cycling tests was estimated to be within several percent for both mPR-9 and mPR-CB-9. These results indicate that the carbon honeycombs can effectively withstand the high pressure associated with high-flux operation and remain structurally stable during repeated adsorption–desorption processes. The minimal mechanical degradation highlights the strong carbon framework formed during heat treatment and the excellent chemical stability against RhB, ethanol, and water. Compared to the thermal regeneration method, this approach offers a more efficient and less energy-intensive regeneration process. Additionally, its ability to restore adsorption capacity without structural degradation ensures long-term durability, making it highly suitable for practical applications that require continuous and reliable performance.

2.5. Energy-efficient heat exchange

Heat exchange is essential in various industrial and domestic applications,[78,79] where efficient energy utilization can reduce energy consumption and improve sustainability. However, traditional heating devices often suffer from significant energy losses during electrical-to-thermal energy conversion. The microhoneycomb-structured carbon monoliths developed in this study are expected to address these issues by providing a large surface area for contact with the working fluid. Carbon possesses moderate electrical resistivity, enabling it to generate Joule heat when direct current is applied. This characteristic has made it a common material for heating elements in high-temperature furnaces. By combining this property with its high thermal conductivity and the efficient heat transfer enabled by the microhoneycomb structure, carbon microhoneycombs are

expected to function as efficient media for direct heating of flowing fluids. To validate this concept, we conducted a proof-of-concept experiment demonstrating heat exchange between flowing water and a Joule-heated carbon microhoneycomb.

To evaluate the intrinsic electrothermal properties, we applied 5 V to mPR-9 in an open-air environment and monitored its surface temperature over time. As shown in Fig. 6a, the sample had a temperature rise, stabilizing at 35–36 °C within 3 min. This result demonstrates that mPR-9 not only exhibits electrical conductivity but also converts electrical energy into heat, making it a promising candidate for electrothermal applications. Beyond electrothermal heating in air, we further investigated the heat exchange efficiency (E_{ex}) of mPR-9 in a dynamic water flow system. As illustrated in Fig. 6b, the testing sample was placed in a water channel with a constant flow rate of 5 mL min^{-1}, and a voltage was applied to its two ends to introduce heat. The inlet and outlet water temperatures were recorded by a thermometer. As shown in Fig. 6c, upon applying voltage, the water temperature started increasing after about 10 s. The initial delay is attributed to the transit time required for the water to flow through the tubing before reaching the heated region. At 30 s, the water temperature increased by 0.9 °C, demonstrating the heat exchange capability. For comparison, we tested a commercial metal honeycomb counterpart with a diameter of *ca.* 9.5 mm, a thickness of *ca.* 9 mm, and a channel size of *ca.* 300 μm (the optical image is shown in Fig. S13). Upon applying voltage, the water temperature increase began after 15 s, slightly slower than mPR-9, and after 60 s, the water temperature had increased by 0.8 °C. This indicates that mPR-9 outperforms the commercial counterpart by achieving faster heat transfer. The superior heat exchange rate of mPR-9 is attributed to its unique structural features. Its high macropore surface area maximizes contact between water and the solid surface, facilitating efficient heat transfer. Additionally, its well-defined microchannels allow unobstructed water flow, minimizing resistance and promoting continuous heat exchange.

To quantify its energy efficiency, the energy input and output of mPR-9 with the commercial counterpart over 60 s were compared. The power consumption during the heat exchange process was compared. As shown in Fig. 6d, the power consumption (yellow area) of mPR-9 was controlled between 0.8–1.25 J s^{-1} with a total energy input (E_{in}) of 60.8 J over 60 s. The energy output (E_{out}), as illustrated in the blue area, was calculated based on the water temperature increase, reaching 13.0 J, resulting in an E_{ex} of 21.4%. In contrast, the commercial counterpart exhibited significantly lower efficiency. As shown in Fig. 6e, despite its higher energy input (2–2.5 J s^{-1}) with an E_{in} (gray area) of 138.9 J over 60 s, its E_{out} was only 7.0 J, leading to an E_{ex} of 5.0%. This means that mPR-9 achieves nearly 4 times higher efficiency in transferring electricity to heat. The results demonstrate that mPR-9 is a highly efficient heat exchanger, offering rapid heating response, lower energy consumption, and superior thermal transfer efficiency compared to commercial products.

To further assess the long-term electrothermal durability of mPR-9, cyclic Joule heating tests were conducted with
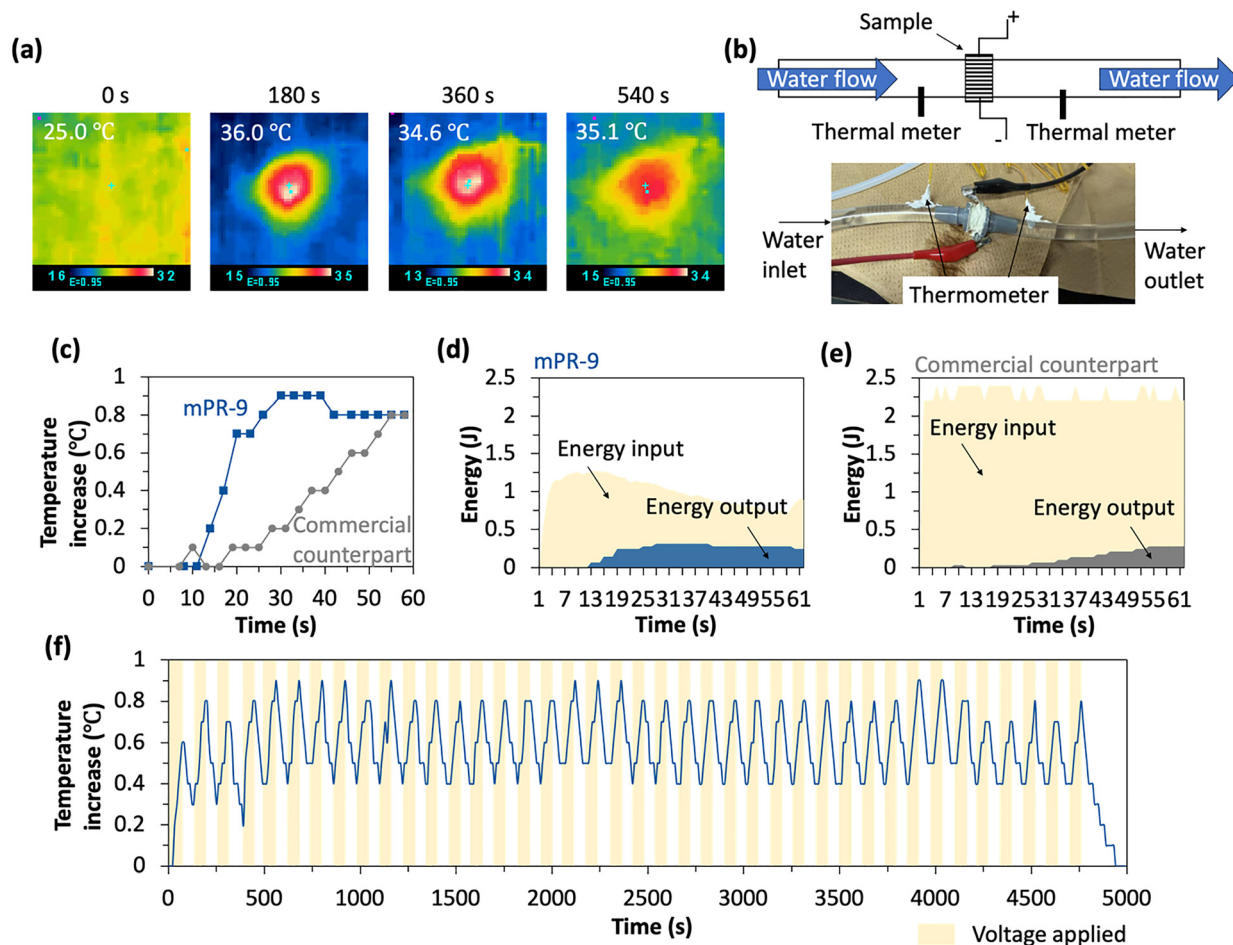
Fig. 6 Electrothermal performance and heat exchange efficiency. (a) Thermal images showing the temperature evolution of mPR-9 under a 5 V applied voltage in an open-air environment at 0 s, 180 s, 360 s, and 540 s. (b) Schematic illustration (top) and optical image (bottom) of the setup for dynamic water heating tests. (c) Water temperature increases over time upon voltage application. (d) Energy input and output of mPR-9 during the heat exchange process. (e) Energy input and output of the commercial counterpart during the heat exchange process. (f) Joule heating stability of mPR-9 under cyclic voltage application. The highlighted regions indicate periods when voltage was applied.

continuous voltage on and off operation. Each cycle consisted of 1 min of voltage application followed by 1 min of resting interval. As shown in Fig. 6f, at 5 V and a water flow rate of 5 mL min^{-1}, mPR-9 maintained a stable temperature response during 40 cycles, with a nearly constant temperature increase (0.8–0.9 °C) in each cycle. The robust carbon framework and continuous conductive network ensured high stability under repeated thermal stress. These results reveal excellent electrothermal reliability for long-term operation.

3. Conclusion

In this study, carbon macroporous monoliths equipped with honeycomb channel arrays were successfully fabricated by incorporating PR and CB into CNF dispersion, followed by ice-templating and heat treatment. The heat treatment at 900 °C leads to the formation of a continuous 3D carbon matrix. This transformation results in a robust carbon network, significantly enhancing the mechanical strength. The carbon

monoliths, mPR-9 and mPR-CB-9, exhibited high compression strengths of 3400 and 1860 kPa with low densities of 0.09 and 0.11 g cm^{-3}, respectively, outperforming most carbon porous materials. To highlight the multifunctionality, we demonstrated two key applications. First, by taking advantage of the excellent mechanical strength, large macropore surface area, and low pressure drop enabled by its straight channels, we achieved rapid purification of RhB-contaminated water at an extremely high flux exceeding 20 000 L m^{-2} h^{-1}. Furthermore, the carbon monoliths can be easily regenerated by flowing ethanol and water, without a decline in RE and flux, highlighting the excellent reusability. Second, their inherent ability to generate Joule heat, combined with their thermal conductivity, enabled highly efficient heat exchange. mPR-9 achieved an energy exchange efficiency of 21.4%, which is four times higher than that of a commercial counterpart (5.0%). These results underscore the multifunctionality of the carbon monoliths, demonstrating their outstanding performance in both adsorption and regeneration for water purification, as well as their high efficiency in heat exchange. Due to their unique structural and functional

characteristics, these materials have great potential for practical applications in environmental remediation and sustainable thermal management systems.

4. Experimental section/methods

4.1. Preparation of precursors

CNF aqueous dispersions (2 wt%, fiber length: *ca.* 200 nm, fiber diameter: *ca.* 30 nm, DKS Co. Ltd) were mixed with phenol formaldehyde resin (*ca.* 45 wt%, number-average molecular weight: 300–600 g mol^{-1}, PHENOLITE 8121-LV, DIC Corporation), and carbon black (Aqua-Black®, *ca.* 20 wt%, particle size *ca.* 50 nm, Tokai Carbon Co., Ltd) at ratios of CNF : PR : CB = 1 : 0 : 0, 1 : 3 : 0, 1 : 0 : 3, 1 : 3 : 3, and 0 : 1 : 1. The composite dispersions were mixed by a homogenizer (T18 digital ULTRA-TURRAX, IKA) at a rotation speed of 10k rpm. Then, the mixed dispersions were defoamed with a conditioning mixer (ARE-250, Thinky Inc.) at 1000 rpm for 5 min. Subsequently, the well-mixed precursors were transferred to polypropylene (PP) tubes for unidirectional freezing.

4.2. Preparation of honeycomb monoliths

Firstly, the PP tubes containing precursor sols were affixed to a dip-coater and slowly immersed in liquid nitrogen (−196 °C) at a constant rate (10 cm h^{-1}). After the samples were completely frozen, they were divided into monoliths with 10 mm by a loop wire saw (EiResearch Co., Ltd, model type: ELW-201). The frozen samples were subsequently freeze-dried at a temperature range of −5 to 25 °C under vacuum conditions. After the freeze-drying process finished, sample surfaces were cleaned with tape to remove impurities.

4.3. Carbonization of honeycomb monoliths

The freeze-dried samples were placed on a quartz plate and put in a vertical furnace with an inner size of *ca.* 54 mm. N$_2$ gas was flowed to the furnace at a flow rate of 1000 mL min^{-1}, replacing the inner gas for 10 min prior to heat treatment. The temperature was then increased to 900 °C at a rate of 10 °C min^{-1} and kept for 1 h while maintaining the N$_2$ flow. The samples were taken out after cooling down below 40 °C.

4.4. Characterization methods

SEM observation. The SEM images were taken using a field emission scanning electron microscope (FE-SEM, S-4800, Hitachi) under an accelerating voltage of 1 kV.

The particle size distribution of the CB dispersion was obtained using the laser diffraction/scattering method (Microtrac MT3300EXII, NIKKISO Co., Ltd).

Thermal analysis for the heat treatment was conducted using a thermogravimeter-differential scanning calorimeter (TG-DSC, STA 449 Jupiter, Netzsch) from 60 °C to 900 °C with a heating rate of 10 °C min^{-1} under a He flow (150 mL min^{-1}). The emission gas from the TG-DSC was analyzed with a quadrupole mass spectrometer (MS, JMS-G1500GC, JEOL).

In situ FT-IR spectra were obtained using a Fourier Transform Infrared Spectrometer (IRSpirit, Shimadzu Corp.). The sample was heated in an Ar atmosphere with a gas flow rate of 100 mL min^{-1}. The temperature range was RT–900 °C. The spectra were detected every 100 °C, and the measurements were conducted over 30 s at a stable temperature. The wavenumber ranged from 500 to 4000 cm^{-1}, and the cumulative number was 30.

An FT-IR spectrum of the CB dispersion was recorded using a Fourier Transform Infrared Spectrometer (FT/IR-6600, JASCO Corporation). The measurement was conducted over a wavenumber range of 400–4000 cm^{-1} with 64 accumulations.

Sample mechanical strengths were tested by a universal testing machine (AGS-X, SHIMADZU Corporation). Samples were compressed in the direction along and perpendicular to the freezing direction to 80% deformation at a compression rate of 100% strain min^{-1}.

N$_2$ adsorption–desorption isotherms were obtained at 77 K (MicrotracBEL Corp. BELSORP-mac). The Brunauer–Emmett–Teller (BET) surface area was calculated using the multipoint BET method from the adsorption data in the range of p/p_0 = 0.01–0.05. The pore size distribution of CB was calculated with the non-local density functional theory (NLDFT) using a slit-pore model.

UV spectra were used to determine the concentration of the pollutant solution by an Ultraviolet/Visible Spectrometer (V-670, JASCO Corporation). The wavelength was from 350–650 nm.

4.5. Dye adsorption isotherms

To each of the six glass vials, 10 mL of RhB solution at concentrations of 10, 20, 50, 100, 200, and 500 mg L^{-1} were added. Next, several amounts of crushed carbon monolith powder were added to each vial. All samples were capped and stirred by a magnetic stir bar at 25 °C for 72 h to reach equilibrium. Next, the samples were removed by filtering through 0.2 μm hydrophilic PTFE syringe filters. The resulting RhB solutions were diluted and analyzed by UV-vis spectroscopy to determine the concentration of RhB solutions. The dilution procedures are as follows:

10 mg L^{-1}: 1 mL RhB solution added to 1 mL deionized water

20 mg L^{-1}: 1 mL RhB solution added to 3 mL deionized water

50 mg L^{-1}: 1 mL RhB solution added to 9 mL deionized water

100 mg L^{-1}: 0.5 mL RhB solution added to 7.5 mL deionized water

200 mg L^{-1}: 0.5 mL RhB solution added to 15 mL deionized water

500 mg L^{-1}: 0.1 mL RhB solution added to 10 mL deionized water

The residual dye concentration (C_e, mg L^{-1}) was calculated according to eqn (2):

$$C_e = \left(\frac{\mathrm{Abs}_E}{\mathrm{Abs}_C}\right) \times [\text{control concentration}] \qquad (2)$$

where Abs_E is the absorption of experimental samples, and Abs_C is the absorption of the control.

Then, the RhB adsorption amount (Q_e, mg g^{-1}) was calculated according to eqn (3):

$$Q_e = \frac{([\text{Control concentration}] - C_e) \times \text{volume}(L)}{\text{Mass of sample}(g)} \quad (3)$$

The RhB adsorption isotherms were fitted to the Langmuir adsorption model using non-linear least squares regression of eqn (4):[68]

$$\frac{1}{Q_m} = \frac{1}{Q_m} + \frac{1}{C_e \times Q_m \times K_L} \quad (4)$$

where Q_m (mg g^{-1}) is the maximum adsorption capacity at equilibrium, and K_L (L mg^{-1}) is the Langmuir equilibrium constant.

4.6. RhB purification tests

As illustrated in Fig. S9, the test sample was fixed on a sample holder and placed on a clean vial. A syringe containing 10 mL of RhB solution (*ca.* 4 mg L^{-1}) was then injected into the sample holder to release the liquid. The concentrations of the filtrates were determined by UV-vis spectroscopy at a wavelength of 554 nm. The removal efficiency (RE) was calculated according to eqn (5):

$$RE = \frac{C_0 - C}{C_0} \times 100\% \quad (5)$$

where C_0 represents the initial concentration of RhB solution, and C is the concentration after purification.

As for the regeneration of carbon monoliths, 10 mL ethanol was flowed through the sample holder at 60 mL min^{-1}, followed by 10 mL water at the same flow rate.

4.7. Heat evolution in an open-air environment

A 5 V voltage was applied to the sample by a power supply (PWR800H, Kikusui), while the surface temperature was monitored by a thermography camera (TIM-03, AS ONE Corporation). Thermal images were captured every 10 s to track the temperature evolution.

4.8. Heat exchange in a dynamic water flow system

As displayed in Fig. 6b, the samples were fixed on two sample holders by silicone rubber and connected to the water channel. The water flow was controlled by a water pump (Q-100-TT-P-S, Tacmina Corporation).

The total energy output was calculated according to eqn (6):

$$E_{out} = mc\Delta T \quad (6)$$

where m is the mass of water, c is the specific heat capacity of water (4.18 J g^{-1} °C^{-1}), and ΔT is the water temperature change.

The heat exchange efficiency (E_{ex}) was calculated according to eqn (7):

$$E_{ex} = \frac{E_{out}}{E_{in}} \times 100\% \quad (7)$$

Author contributions

Minghao Liu: conceptualization, investigation, methodology, and writing – original draft. Masataka Inoue: conceptualization and methodology. Hirotaka Nakatsuji: investigation and supervision. Rui Tang: conceptualization, investigation, and methodology. Zheng-Ze Pan: conceptualization, investigation, and methodology. Hirotomo Nishihara: funding acquisition, investigation, methodology, supervision, and writing – review and editing.

Conflicts of interest

There are no conflicts to declare.

Data availability

The data supporting this article have been included as part of the supplementary information (SI). Supplementary information: Fig. S1, schematic illustration of ice crystal growth, Fig. S2, particle dispersion of carbon black, Fig. S3, SEM image of ice-templated sample from only PR and CB and illustration of ice growth without CNF, Fig. S4, optical images of directly dried unidirectionally frozen samples, Fig. S5, morphology changes of mCNF by carbonization, Fig. S6, FT-IR spectrum of CB, Fig. S7, an enlarged view of the initial linear region of Young's moduli in Fig. 4, Fig. S8, high-resolution SEM images of carbonized honeycombs, Fig. S9, radical compression stress–strain curves of mPR, mPR-9 and mPR-CB-9, Fig. S10, porosity characteristics of CB, Fig. S11, calibration of RhB, Fig. S12, illustration of the setup for RhB filtration, Fig. S13, optical image of commercial metal-based honeycomb monolith. See DOI: https://doi.org/10.1039/d5mh01458a.

Acknowledgements

Notes and references

1 I. Mattich, A. Ofner and A. R. Studart, *Adv. Eng. Mater.*, 2025, **27**, 2401363.

2 B. Wang, P. Prinsen, H. Wang, Z. Bai, H. Wang, R. Luque and J. Xuan, *Chem. Soc. Rev.*, 2017, **46**, 855–914.

3 K. Takahashi, S. Yoshida, K. Urkasame, S. Iwamura, I. Ogino and S. R. Mukai, *Adsorption*, 2019, **25**, 1241–1249.

4 X. Peng, L. Chen and Y. Li, *Mol. Catal.*, 2022, **529**, 112568.

5 M. A. Usman and A. Y. Khan, *J. Hazard. Mater.*, 2022, **428**, 128238.

6 M.-Q. Zhao, X. Xie, C. E. Ren, T. Makaryan, B. Anasori, G. Wang and Y. Gogotsi, *Adv. Mater.*, 2017, **29**, 1702410.

7 M. Liu, Z.-Z. Pan, M. Ohwada, R. Tang, H. Matsui, M. Tada, M. Ito, A. Ikura and H. Nishihara, *ACS Appl. Mater. Interfaces*, 2024, **16**, 29177–29187.

8 H. Wang, S. Tan, Z. Su, M. Li, X. Hao and F. Peng, *Adv. Mater.*, 2024, **36**, 2311073.

9 Y. Hatakeyama, H. Naito, R. Oda and S. Shiraishi, *J. Energy Storage*, 2024, **91**, 111974.

10 H. Itoi, G. Saeki, T. Usami, S. Takagi, H. Suzuki, T. Ishii, H. Iwata and Y. Ohzawa, *ACS Sustainable Resour. Manage.*, 2024, **1**, 743–756.

11 D. Tanaka, N. Takemori, Y. Iba, K. Suyama, S. Shimizu, T. Yoshii, H. Nishihara, Y. Kamimura, Y. Kubota and S. Inagaki, *Microporous Mesoporous Mater.*, 2024, **379**, 113294.

12 H. Ando, K. Hashi, S. Ohki, Y. Hatakeyama, Y. Nishina, N. Kowata, T. Ohkubo and K. Gotoh, *Carbon Trends*, 2024, **16**, 100387.

13 Y. Ito, C. Lee, Y. Miyahara, K. Miyazaki and T. Abe, *ACS Energy Lett.*, 2024, **9**, 1473–1479.

14 K. Ishii, T. Ogiyama, K. Fumoto and Y. Nishina, *Appl. Phys. Lett.*, 2024, **125**, 023104.

15 T. Tomaru, H. Shimanoe, S. Hong, S.-J. Ha, Y.-P. Jeon, K. Nakabayashi, J. Miyawaki and S.-H. Yoon, *Carbon*, 2024, **226**, 119160.

16 W. Yu, Z. Shen, T. Yoshii, S. Iwamura, M. Ono, S. Matsuda, M. Aoki, T. Kondo, S. R. Mukai, S. Nakanishi and H. Nishihara, *Adv. Eng. Mater.*, 2024, **14**, 2303055.

17 K. Kira, T. Yamamoto, Y. Sugimoto, I. Shimabukuro, A. Hikosaka and T. Irisawa, *Carbon*, 2024, **228**, 119417.

18 J. Wang, Y. Yao, C. Zhang, Q. Sun, D. Cheng, X. Huang, J. Feng, J. Wan, J. Zou, C. Liu and C. Yu, *Adv. Sci.*, 2021, **8**, 2100120.

19 R. Liu, Q. Wan, Y. Yu, X. Zhang, L. Liu, H. Wang and C. Yue, *J. Water Process Eng.*, 2023, **53**, 103659.

20 A. I. Douka, Y. Xu, H. Yang, S. Zaman, Y. Yan, H. Liu, M. A. Salam and B. Y. Xia, *Adv. Mater.*, 2020, **32**, 2002170.

21 Y. Wang, L. Zhang, H. Hou, W. Xu, G. Duan, S. He, K. Liu and S. Jiang, *J. Mater. Sci.*, 2021, **56**, 173–200.

22 H. Nishihara, S. R. Mukai, D. Yamashita and H. Tamon, *Chem. Mater.*, 2005, **17**, 683–689.

23 H. Nishihara, S. Iwamura and T. Kyotani, *J. Mater. Chem.*, 2008, **18**, 3662–3670.

24 S. Deville, E. Saiz, R. K. Nalla and A. P. Tomsia, *Science*, 2006, **311**, 515–518.

25 S. Deville, *Adv. Eng. Mater.*, 2008, **10**, 155–169.

26 Z.-Z. Pan, H. Nishihara, S. Iwamura, T. Sekiguchi, A. Sato, A. Isogai, F. Kang, T. Kyotani and Q.-H. Yang, *ACS Nano*, 2016, **10**, 10689–10697.

27 Z.-Z. Pan, W. Lv, Q.-H. Yang and H. Nishihara, *Bull. Chem. Soc. Jpn.*, 2022, **95**, 611–620.

28 Z.-Z. Pan, H. Nishihara, W. Lv, C. Wang, Y. Luo, L. Dong, H. Song, W. Zhang, F. Kang, T. Kyotani and Q.-H. Yang, *J. Visualized Exp.*, 2018, 57144.

29 Y. Fei, M. Liang, L. Yan, Y. Chen and H. Zou, *Chem. Eng. J.*, 2020, **392**, 124815.

30 M. Shen, J. Qi, K. Gao, C. Duan, J. Liu, Q. Liu, H. Yang and Y. Ni, *Chem. Eng. J.*, 2023, **464**, 142719.

31 Z. Zhang and X.-Y. Liu, *Chem. Soc. Rev.*, 2018, **47**, 7116–7139.

32 S. Deville, S. Meille and J. Seuba, *Sci. Technol. Adv. Mater.*, 2015, **16**, 043501.

33 Q. Zhang, X. Yang, P. Li, G. Huang, S. Feng, C. Shen, B. Han, X. Zhang, F. Jin, F. Xu and T. J. Lu, *Prog. Mater. Sci.*, 2015, **74**, 332–400.

34 R. Tang, Z.-Z. Pan, M. Liu, M. Ohwada and H. Nishihara, *Nano Res.*, 2023, **16**, 8018–8024.

35 Z.-Z. Pan, A. Govedarica, H. Nishihara, R. Tang, C. Wang, Y. Luo, W. Lv, F.-Y. Kang, M. Trifkovic and Q.-H. Yang, *Small*, 2021, **17**, 2005564.

36 L. Solhi, V. Guccini, K. Heise, I. Solala, E. Niinivaara, W. Xu, K. Mihhels, M. Kröger, Z. Meng, J. Wohlert, H. Tao, E. D. Cranston and E. Kontturi, *Chem. Rev.*, 2023, **123**, 1925–2015.

37 J. Lu, M. Yuan, X. Di, Q. Yuan, L. Ni, Y. Luo, Y. Chen and H. Zou, *Chem. Eng. J.*, 2024, **489**, 151385.

38 J. Ozaki, W. Ohizumi and A. Oya, *Carbon*, 2000, **38**, 1515–1519.

39 H. Jiang, J. Wang, S. Wu, Z. Yuan, Z. Hu, R. Wu and Q. Liu, *Polym. Degrad. Stab.*, 2012, **97**, 1527–1533.

40 K. A. Trick and T. E. Saliba, *Carbon*, 1995, **33**, 1509–1515.

41 J. Levanič, M. Gericke, T. Heinze, I. Poljanšek and P. Oven, *Cellulose*, 2020, **27**, 2053–2068.

42 X. Sang, C. Qin, Z. Tong, S. Kong, Z. Jia, G. Wan and X. Liu, *Cellulose*, 2017, **24**, 2415–2425.

43 S. Fujisawa, Y. Okita, H. Fukuzumi, T. Saito and A. Isogai, *Carbohydr. Polym.*, 2011, **84**, 579–583.

44 S. Feng, Z. Yuan, M. Leitch and C. C. Xu, *Ind. Crops Prod.*, 2015, **76**, 258–268.

45 M. K. Alam, M. T. Islam, M. F. Mina and M. A. Gafur, *J. Appl. Polym. Sci.*, 2014, **131**(13), 40421.

46 A. Beda, P.-L. Taberna, P. Simon and C. Matei Ghimbeu, *Carbon*, 2018, **139**, 248–257.

47 J. Simitzis, L. Zoumpoulakis, S. Soulis, D. Triantou and C. Pinaka, *J. Appl. Polym. Sci.*, 2011, **121**, 1890–1900.

48 Y. He, R. Duan, Q. Zhang, T. Xia, B. Yan, S. Zhou and J. Huang, *Adv. Compos. Hybrid. Mater.*, 2021, **4**, 317–323.

49 Z. Li, Q. Yang, R. Fang, W. Chen and H. Hao, *Thin-Walled Struct.*, 2021, **160**, 107365.

50 R. D. Hussein, D. Ruan, G. Lu, S. Guillow and J. W. Yoon, *Thin-Walled Struct.*, 2017, **110**, 140–154.

51 H. Wang, Z. Chen and D. Su, *J. Mater. Sci. Technol.*, 2024, **179**, 145–154.

52 C. Chen, X. Zhu and B. Chen, *Chem. Eng. J.*, 2018, **354**, 896–904.

53 L. Qiu, J. Z. Liu, S. L. Y. Chang, Y. Wu and D. Li, *Nat. Commun.*, 2012, **3**, 1241.

54 W. Li, L. Feng, X. Shi and Y. Wang, *Adv. Eng. Mater.*, 2021, **23**, 2100452.

55 C. Banerjee, V. K. Chandaliya, P. S. Dash and B. C. Meikap, *Diamond Relat. Mater.*, 2019, **95**, 83–90.

56 B. Wicklein, A. Kocjan, G. Salazar-Alvarez, F. Carosio, G. Camino, M. Antonietti and L. Bergström, *Nat. Nanotechnol.*, 2015, **10**, 277–283.

57 X. Li, S. Liu, Y. Huang, Y. Zheng, D. P. Harper and Z. Zheng, *ACS Sustainable Chem. Eng.*, 2018, **6**, 3515–3524.

58 C. J. Zúñiga Ruiz, A. Szczurek, A. Martínez de Yuso Arisa, J. C. Ronda, V. Cádiz, V. Fierro and A. Celzard, *Carbon*, 2015, **95**, 919–929.

59 X. Chen, H. Liu, Y. Zheng, Y. Zhai, X. Liu, C. Liu, L. Mi, Z. Guo and C. Shen, *ACS Appl. Mater. Interfaces*, 2019, **11**, 42594–42606.

60 Y. Yang, Z. Tong, T. Ngai and C. Wang, *ACS Appl. Mater. Interfaces*, 2014, **6**, 6351–6360.

61 J. Yang, S. Li, Y. Luo, L. Yan and F. Wang, *Carbon*, 2011, **49**, 1542–1549.

62 X. Zhou, Y. Wang, L. Xiao, M. Zhang, Z. Su and Q. Huang, *Compos. Commun.*, 2023, **37**, 101460.

63 Z. Chen, H. Zhuo, Y. Hu, H. Lai, L. Liu, L. Zhong and X. Peng, *Adv. Funct. Mater.*, 2020, **30**, 1910292.

64 D. Liu, G. Zhang, T. Cao, K. Gui, M. Wang, W. Han and A. Wang, *Vacuum*, 2022, **205**, 111478.

65 M. M. G. Sow, Z. Zhang, C. H. Sow and S. X. Lim, *Nat. Commun.*, 2023, **14**, 6508.

66 A. Alsbaiee, B. J. Smith, L. Xiao, Y. Ling, D. E. Helbling and W. R. Dichtel, *Nature*, 2016, **529**, 190–194.

67 S. Kandambeth, B. P. Biswal, H. D. Chaudhari, K. C. Rout, S. Kunjattu, H. S. Mitra, S. Karak, A. Das, R. Mukherjee, U. K. Kharul and R. Banerjee, *Adv. Mater.*, 2017, **29**, 1603945.

68 J. L. Fenton, D. W. Burke, D. Qian, M. Olvera de la Cruz and W. R. Dichtel, *J. Am. Chem. Soc.*, 2021, **143**, 1466–1473.

69 L. M. Skjolding, L. G. Jørgensen, K. S. Dyhr, C. J. Köppl, U. S. McKnight, P. Bauer-Gottwein, P. Mayer, P. L. Bjerg and A. Baun, *Water Res.*, 2021, **197**, 117109.

70 A. A. Al-Gheethi, Q. M. Azhar, P. Senthil Kumar, A. A. Yusuf, A. K. Al-Buriahi, R. M. S. Radin Mohamed and M. M. Al-shaibani, *Chemosphere*, 2022, **287**, 132080.

71 X. Zhu, K. Zhang, N. Lu and X. Yuan, *Appl. Surf. Sci.*, 2016, **361**, 72–79.

72 K. Dey, M. Pal, K. C. Rout, S. Kunjattu H, A. Das, R. Mukherjee, U. K. Kharul and R. Banerjee, *J. Am. Chem. Soc.*, 2017, **139**, 13083–13091.

73 S. Saja, A. Bouazizi, B. Achiou, H. Ouaddari, A. Karim, M. Ouammou, A. Aaddane, J. Bennazha and S. Alami Younssi, *J. Eur. Ceram. Soc.*, 2020, **40**, 2453–2462.

74 N. Shao, S. Tang, S. Li, H. Chen and Z. Zhang, *J. Hazard. Mater.*, 2020, **388**, 121736.

75 Q. Chen, P. Yu, W. Huang, S. Yu, M. Liu and C. Gao, *J. Membr. Sci.*, 2015, **492**, 312–321.

76 J. Hu, H. Zhu, M. Lin, D. Wu, J. Yao, T. Sun, X. Ma and Y. Xia, *J. Electroanal. Chem.*, 2023, **946**, 117742.

77 Y. Yue, K. Hou, J. Chen, W. Cheng, Q. Wu, J. Han and J. Jiang, *ACS Appl. Mater. Interfaces*, 2022, **14**, 24708–24719.

78 L. E. Bell, *Science*, 2008, **321**, 1457–1461.

79 Z. Li, Z. Lin, M. Han, Y. Mu and J. Yu, *J. Mater. Sci.*, 2021, **56**, 14542–14555.